Research Article

Enhancing spatial resolution in magnetic particle imaging using eigen-reconstructions: opportunities and limitations

Jorge Chacon-Caldera [a,*] · Heinrich Lehr [a] · Kulthisa Sajjamark [a] · Jochen Franke [a]

[a]Bruker BioSpin MRI GmbH, Ettlingen, Germany
*Corresponding author, email: jorge.chacon_caldera@bruker.com

Abstract

Enhancements in spatial resolution can open new avenues for novel applications, but acquiring data at higher resolutions generally comes with penalties in measurement times, signal-to-noise ratios and safety concerns. Therefore, maximizing the spatial resolution of the available data during image reconstruction is paramount. Magnetic Particle Imaging (MPI) has already reached sub-millimeter spatial resolutions. With standard tracers, this has been achieved using a reconstruction method that compensates for the point spread function of the system and the superparamagnetic iron oxide particles (SPIOs). This method is known as the system matrix approach and uses a calibration measurement, relating the concentration of SPIOs and the true particle response to the measured signal. Using a calibration measurement for reconstruction requires a comprehensive assessment of the quality of the system matrix in addition to the measured image data. Analyzing the system matrix by reconstructing selected measurements contained in itself and visualizing them in image space (henceforward called eigen-reconstructions) can provide clear information regarding image quality and artifacts. This is equivalent to using ideal measurement data. Thus, it is possible to identify sources of image artifacts arising solely from the reconstruction, which can be then compensated. In a preliminary report, we presented the principle of eigen-reconstructions to identify and reduce reconstruction-induced artifacts. In this work, we focus on the application of the method to enhance spatial resolution in MPI reconstructions. The principles of an iterative algorithm based on eigen-reconstructions are also further detailed. It is shown that the algorithm compensates the blur arising during image reconstruction effectively. For validation, we present tests of our method using 2D and 3D datasets including an homogeneous and a resolution phantom to demonstrate potential opportunities and limitations.

I. Introduction

In biomedical imaging, enhancements in spatial resolution open new avenues to investigate smaller structures and obtain more detailed anatomical and physiological information. In Magnetic Particle Imaging (MPI), alongside cardio-vascular [1, 2], kidney imaging is a very promising application since its tracers are safe for chronic kidney disease patients [3, 4]. Using MPI, it could

be possible to quantify important parameters for renal function, such as perfusion, with high temporal resolution. However, this could be soon achieved safely in humans with magnetic resonance imaging using novel contrast agents, e.g. hyperpolarized xenon-129 [5]. And, while perfusion is a good indicator for deterioration in renal function, the number of nephrons in the kidney could be a more accurate and even a predictive indicator

of renal failure. For this purpose, the quantification of individual functional nephrons in mouse kidneys has been demonstrated using cationized-ferritin at resolutions of tens of micrometers with ultra high field magnetic resonance imaging [6, 7]. Enhancing the spatial resolution in MPI could make it a more suitable candidate for this type of application due to its higher sensitivity and quantitative nature. However, acquiring native data with higher resolutions generally leads to additional costs in terms of reduced signal-to-noise ratios and increased scan times. Specifically in MPI, enhancing the resolution during data acquisition involves the use of higher gradient selection field (SF) strengths. Additionally, the sampled field-of-view (FoV) is given by the ratio of (twice) the amplitude of the oscillating drive field (DF) and the static gradient SF. This requires the DF to be increased in order to maintain a desired FoV with a higher resolution. In MPI, a typical combination of field strengths are in the order of a few T/m for the SF and tens of mT for the DF. Achieving these combinations is not only technically challenging, but also, could have a negative impact in terms of safety. This is due to the increased specific absorption rate and risks of peripheral nerve stimulation [8]. On the other hand, maximizing spatial resolution of the acquired data during reconstruction involves only computational costs. Therefore, evaluating and reducing negative impacts of the reconstruction on spatial resolution is highly desirable.

In this work, we extend our preliminary report [9] to enhance spatial resolution in MPI images. Our approach relies on the reduction of blur added during reconstructions based on the system matrix approach. For this, we take selected measurements from the system matrix (MPI measurements with a delta probe at different locations) and reconstruct them as test images using the same system matrix. Thus, performing what we have termed *eigen-reconstructions* of the system matrix. This aids assessing the quality and artifacts of the system matrix and reconstruction method. We test different reconstruction parameters and identify cases where artifacts are present as blurring. We then use a purpose-developed algorithm to reduce blurring using information from the eigen-reconstructions. The opportunities and limitations of the method are demonstrated in 2D and 3D datasets of various phantoms. We include tests on an homogeneous phantom using two system matrices acquired with different number of points and showing different levels of blurring in their eigen-reconstructions. Moreover, we demonstrate the performance of the de-blurring algorithm for various reconstruction parameters and signal-to-noise ratio (SNR) levels in the data using a resolution phantom.

II. Theory

MPI continues establishing itself as a powerful modality due to its set of remarkable advantages such as high sampling efficiency and sub-millimeter spatial resolution. In terms of sampling efficiency, Lissajous trajectories have enabled the acquisition of whole 3D volumes in ca. 21 milliseconds [1]. These trajectories sample volumes using variable densities and velocities depending on spatial location. They also generate multifactorial responses of the superparamagnetic iron oxide particles (SPIOs) necessary to generate the MPI signal. For instance, the SPIOs' responses not only follow the Langevin function as response of an instantaneous magnetic field strength, but they also show dependency on drive frequency, temperature, viscosity, etc. Consequently, these responses are difficult to predict and cause the image reconstruction of these signals to be non-trivial. One solution employed for reconstruction is the use of a calibration measurement to characterize the system and particles' responses. This process uses a small delta-type sample scanned at several discrete spatial locations, yielding the so-called system matrix [10]. In this case, the system matrix is a measured transfer function that relates a measurement (image data) to the object (local SPIO concentration) [11]:

$$\mathbf{SMc} = \mathbf{u}$$

Where **SM** is the system matrix, **c** is the concentration vector (local tracer concentration in the object) and **u** is the measured signal vector. Thereby, an image or a volume can be reconstructed using linear algebra techniques such as the regularized Kaczmarz algorithm [12]:

$$arg.\,min.\,||\mathbf{SMc} - \mathbf{u}||_2^2 + \lambda ||\mathbf{c}||_2^2$$

Where λ is the regularization parameter and $||\cdot||_2^2$ indicates the L^2-norm. This approach is not only robust, but also compensates for uneven sample densities and velocities as well as for the SPIOs' responses. These responses determine the point spread function and thus, the native image resolution which is the derivative of the Langevin function. In terms of image resolution, the system matrix includes the point spread function and allows to compensate for it. Thus, the reconstructed resolution can be higher than the native resolution. However, as a consequence of using measured (non-ideal) data in the system matrix, the reconstructed images will have dependency on the data quality in the system matrix which normally is only assessed by evaluating its SNR in Fourier space [13].

Now, consider that each column of the system matrix is a full measurement acquired with the probe at one spatial location. In this case, it is possible to reconstruct each column independently as a 1D plot, a 2D image or a 3D volume. Reconstructing these vectors using the same system matrix from where they were selected is

the concept of eigen-reconstructions. Formally, this is performed by equating the measurement vector **u** to one desired column n of the system matrix ($\mathbf{SM}(n)$). Thus, the problem for the image reconstruction becomes:

$$\mathbf{u} = \mathbf{SM}(n) \Rightarrow arg.\, min.\, \|\mathbf{SMc} - \mathbf{SM}(n)\|_2^2 + \lambda\|\mathbf{c}\|_2^2$$

Ideally, each of these measurements represents a unique point in space and should be reconstructed as a single pixel or voxel with 100% intensity within the FoV covered by the trajectory. This should be perfectly achieved since the evaluated data has a perfect match of signal and noise in the system matrix. Deviations thereof represent ill-conditions during reconstruction, translating to artifacts in the reconstructed images. Moreover, since the artifacts found in an eigen-reconstruction arise from ill-conditioned reconstructions, they are also expected when reconstructing independent data. This is the principle of our deblurring algorithm which subtracts the blur found in eigen-reconstructions from reconstructed images of independent data.

III. Material and methods

To demonstrate our concept, eigen-reconstructions were performed on MPI measurements available online from the project "open MPI data" [14, 15] with three different system matrices ($\mathbf{SM}_1$, $\mathbf{SM}_2$, and $\mathbf{SM}_3$). 3D data measured in-house was also used with an additional system matrix ($\mathbf{SM}_4$). From the open MPI data project, we used data acquired using a field-free point preclinical MPI system (Bruker BioSpin MRI GmbH, Ettlingen, Germany).

For $\mathbf{SM}_1$, the acquisition parameters were as follows: tracer: volume = 1 μL (c = 0.5 mol/L) Ferucarbotran (Resovist, Bayer Pharma AG, Berlin, Germany), number of averages (NA) = 1500, Bandwidth = 1.25 MHz. The excitation was performed using a 2D Lissajous trajectory with sinusoidal excitation (frequencies: f_x = 2.5 MHz/102, f_y = 2.5 MHz/96) and DF amplitude = 14 mT in each channel. For the SF, the gradient strength was = 1.25 T/m (in x- and y-direction). The system matrix was acquired at 1936 spatial locations using a robot for positioning (44 × 44 point grid) with FoV = 44 × 44 mm^2 (FoV$_{DF}$ = 22 × 22 mm^2).

For $\mathbf{SM}_2$ and $\mathbf{SM}_3$, Perimag (micromod Partikeltechnologie, Rostock, Germany) was used as tracer (volume = 4 μL, c = 0.1 mol/L), the DF amplitude was 12 mT, and the SF gradient strength was 1.0 T/m. $\mathbf{SM}_2$ used a FoV = 38 × 38 × 19 mm^3 and $\mathbf{SM}_3$ a FoV = 37 × 37 × 18.5 mm^3. The center slice of the data in z-direction was used henceforth. The main difference between these two system matrices was their size: $\mathbf{SM}_2$ was acquired with a lower resolution using a grid of 19 × 19 × 19 points, $\mathbf{SM}_3$ was acquired with a grid of 37 × 37 × 37 points.

For the system matrices $\mathbf{SM}_1$, $\mathbf{SM}_2$, and $\mathbf{SM}_3$ and their corresponding test data, image reconstruction was performed with the algorithm described in [16]. This is a regularized Kaczmarz algorithm using x- and y- receive channels with an 80 kHz high-pass filter. No reordering or selection of frequency components based on SNR was performed. Positive and real reconstructed signals were enforced.

In a typical image reconstruction using the system matrix approach, the blurring is largely determined by the number of iterations and the regularization parameter. This presents a trade-off between blurring and noise. We tested these effects in eigen-reconstructions using $\mathbf{SM}_1$ to optimize these reconstruction parameters.

The next goal was to compensate the blur added by the reconstruction in independent measurement data. For this, we developed and implemented a blurring correction algorithm using eigen-reconstructions. The algorithm follows these steps:

1. Reconstruct an image or volume of the independent measurement data using a standard system matrix approach := input

2. Find maximum intensity pixel in the input and store it as an entry of the output matrix: I_{max}(input) $\Rightarrow$ output

3. Select the corresponding location of I_{max}(input) in the system matrix and equate it as measurement vector ($\mathbf{u} = \mathbf{SM}(n)$). Reconstruct the new measurement vector using the same reconstruction parameters as for the input. This yields the eigen-reconstruction of that location := EiR($\mathbf{SM}(n)$)

4. Correct intensity of the eigen-reconstruction and subtract it from the input image. This subtraction will be taken as an updated input for a new iteration: input = input - $\left(\frac{I_{max}(\text{input})}{I_{max}(\text{EiR}(\mathbf{SM}(n)))} \cdot \text{EiR}(\mathbf{SM}(n))\right)$

5. Go to step 2 and iterate while I_{max}(input) > threshold

A schematic of the algorithm can be observed in Figure 1. Due to the subtraction of the input and the eigen-reconstruction, subsequent iterations will loop over high intensity pixels elsewhere in the FoV. More importantly, the subtraction includes, and thus, compensates for the blur of the eigen-reconstruction which also appears in the standard image reconstruction.

The algorithm was tested and compared to standard reconstructions using $\mathbf{SM}_1$ and the measurement (NA = 500) of a 5-point phantom filled with Resovist (point diameter = 1.1 mm, c = 0.5 mol/L, volume = 100 μL) **14**. The threshold value during the correction was modified to show its effect on the output image and to prove that the resulting image is not merely equivalent to applying an intensity threshold on the reconstructed images.

To test further opportunities and limitations of our method, stand-alone eigen-reconstructions and recon-
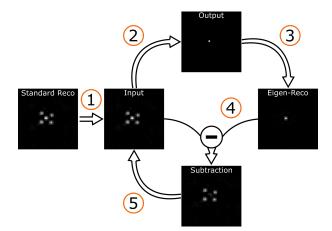
Figure 1: Schematic of the proposed iterative algorithm used for deblurring. The key steps are: 1) using an input image reconstructed with standard system matrix methods, 2) finding the maximum intensity pixel and store it as an entry in the output image, 3) use the maximum intensity pixel and eigen-reconstructing the same position, 4) subtract the eigen-reconstruction (with corrected maximum intensity) from the input image. The subtraction removes the highest intensity voxel and its blur in the input based on the eigen-reconstruction. 5) The subtraction is used as input for a subsequent iteration, correcting another pixel in the FoV. The algorithm iterates over all pixels in the input with a maximum intensity of the input above a desired threshold.

structions with the deblurring algorithm were also evaluated using a phantom in the shape of a cone. The cone was filled with Perimag (c = 0.05 mol/L, volume = 684 μL), had a 1 mm radius tip, an apex angle of 10 degrees and a height of 22 mm. In 2D, the ideal reconstruction of this phantom is approximately a triangle with homogeneous concentration [14]. Image reconstructions of the same measurement data were performed with $\mathbf{SM}_2$ and $\mathbf{SM}_3$.

Finally, the performance of the algorithm with 3D datasets was tested using $\mathbf{SM}_4$. These measurements were taken on a different Bruker preclinical MPI system and an in-house implementation of the regularized Kaczmarz algorithm was used for reconstruction. This was done with the purpose of further validating our approach. There, we used a resolution phantom containing 16 probes filled with Resovist. The probes are cylinders with 2 mm in diameter and 3 mm in height. The separation of the cylinders varied from 1 to 3.5 mm from their respective edges with the minimum separation in x-axis of 1.5 mm and in y-axis of 1 mm [17].

The system matrix ($\mathbf{SM}_4$) was acquired with the following parameters: tracer: undiluted Resovist (Ferucarbotran volume = 27 μL, c = 0.5 mol/L), NA = 100, and Bandwidth = 1.25 MHz. The excitation was performed using a 3D Lissajous trajectory with sinusoidal excitation (f_x = 2.5 MHz/102, f_y = 2.5 MHz/96, f_z = 2.5 MHz/99) and DF amplitude = 14 mT in each direction. For the

SF, the gradient strength was 1.25 T/m (x- = y- = 1/2 z-direction). The system matrix was acquired at 10976 spatial locations using a robot for positioning (28 × 28 × 14 point grid) with FoV = 28 × 28 × 14 mm³ (FoV_{DF} = 22.4 × 22.4 × 11.2 mm³).

Image reconstruction was performed with a regularized Kaczmarz algorithm using x-, y- and z-receive channels with a 30 kHz high-pass filter. Frequency components with SNR lower than 4 were discarded, positive and real reconstructed signals were enforced. Using this resolution phantom, two tests were performed: 1) the effect of the number of iterations and the regularization factor in the Kaczmarz algorithm was investigated. For the test, we used 1 and 5 iterations with 3 regularization factors: 1×10^{-15}, 1×10^{-10} and 1×10^{-1}, and 2) the effect of the number of averages of the independent measurement data was varied to evaluate the effect of different noise levels on the deblurring algorithm. For this test, we used measurement data with NA = 50, 100, 500 and 1000. Plots of the center slice were also taken in x- and y-directions to demonstrate the effect of the deblurring algorithm in comparison to the input image with 1000 averages. Moreover, isosurface plots were also computed from the resulting 3D volumes for the input and output data, as well as a reference reconstruction with 20 iterations.

IV. Results and discussion

In the first eigen-reconstructions, selected measurements in $\mathbf{SM}_1$ were individually reconstructed. These measurements corresponded to different spatially located points along the diagonal of the FoV. The sum of all reconstructions using 1 iteration ($i = 1$) and no regularization ($\lambda = 0$) showed increased blurring with higher signal intensity in the central points (Figure 2, Left). An eigen-reconstruction of every probe position was also performed, yielding 44 × 44 = 1936 images. From these eigen-reconstructions, the maximum intensity pixel was then selected by 1) stacking these images to form a 3D volume (size = 44 × 44 × 1936) and 2) using the function 'max' to return the maximum element along the 3rd dimension. The image in Figure 2, Right was formed following this process. There, a higher intensity was found in pixels located in the area covered by the trajectory vs. outside (mean ± standard deviation): 0.44 ± 0.08 vs. 0.31 ± 0.01. The intensities are not normalized but as the reconstructed vector exists in the system matrix, the eigen-reconstruction is expected to yield a maximum intensity of 1. The values below 1 represent a reconstruction artifact. Moreover, while it is known that signals can be detected beyond the area covered by the trajectory [18], the ability to reconstruct the selected measurements in these areas could be due to the perfect noise match (instead of signal) between the measurement and the system matrix.
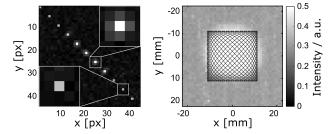
Figure 2: Two representations of eigen-reconstructions SM_1 ($i = 1$, $\lambda = 0$). Left: sum of selected sample positions showing blurring surrounding the center points. Right: maximum intensity pixel of every sample position showing higher intensities within the area of the Lissajous trajectory with respect to the overscanned area.
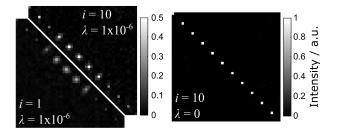

Figure 3: Sum of eigen-reconstructions of sample points from SM_1 located along the diagonal using different reconstruction parameters. On the Left, the number of iterations (i) was increased from 1 to 10. This step increased the intensity of the reconstructed objects but the blurring remained visible. On the Right, the intensity was increased further while the blurring was reduced by setting the regularization factor (λ) to zero.

Figure 4: Results from standard reconstructions compared to the proposed correction algorithm using the regularized Kaczmarz algorithm with SM_1 to reconstruct a 5-point phantom. The input image is obtained with $i = 1$ and $\lambda = 1 \times 10^{-6}$ and the reference is obtained with the parameters optimized using eigen-reconstructions $i = 10$ and $\lambda = 0$.

Figure 5: Applying an intensity threshold on a reconstructed image using a standard approach was not equivalent to correcting with the proposed algorithm using different thresholds (SM_1 used here).

In Figure 3, decreased blurring in eigen-reconstructions was achieved using a lower λ value. Meanwhile, the reconstructed intensity converged to the ideal value of 1 as the number of iterations increased. A virtually ideal reconstruction was achieved when optimizing these factors, demonstrating the first potential use of the eigen-reconstructions: reconstruction parameter optimization.

We then took these optimized reconstruction parameters ($i = 10$ and $\lambda = 0$) as reference. In contrast to the near-ideal eigen-reconstructions obtained with these parameters, reconstructions using independent measurement data showed remaining blur (see Input and Reference in Figure 4). Moreover, the reference image also showed increased noise levels with respect to the input image. This was expected due to the well-known trade-off between resolution and noise arising from the reduced regularization value. The blur in the input and reference images was considerably higher than the one observed in the output image of the proposed algorithm. In the output image, alongside the higher apparent resolution, a lower noise level can be observed given the stopping criterion, which breaks the iteration loop at a selected
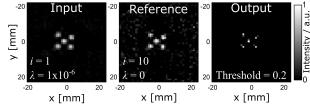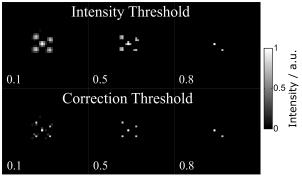
intensity threshold (Output, Figure 4). The threshold was selected to be higher than the background noise (20% of the maximum intensity in the image shown). Since the selected threshold also limits the detection of objects with lower intensity than 20% of the maximum, different threshold values were then investigated. This step aims at assessing the trade-off between object detection and noise rejection.

Three different exemplary threshold selection values are shown in Figure 5. There, evidence is also provided that the correction algorithm is not equivalent to an intensity threshold. It can be observed that the objects are well resolved across a wide range of threshold values (0.1-0.5), which is desired to minimize user bias. Moreover, the intensity threshold deformed the objects whereas our algorithm reconstructed the expected 5 points from the lowest tested threshold value (0.1). On the other hand, as the intensity threshold is initially implemented as hard stopping criterion, this may cause a loss of information for large dynamic ranges. For instance, if a maximum intensity in a volume is produced by a subvolume with large tracer concentration, other subvolumes producing less intensity than the applied threshold will be discarded even if the noise level is lower. An alternative solution to
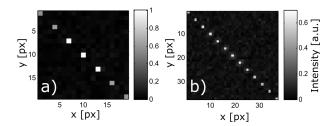
Figure 6: Eigen-reconstructions of $\mathbf{SM}_2$ and $\mathbf{SM}_3$ obtained with Perimag containing two different grid sizes: a) $\mathbf{SM}_2$ with 19×19 and b) $\mathbf{SM}_3$ with 37×37 points. The two system matrices were acquired using the same FoV and overscan.
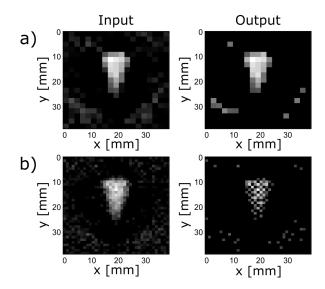

Figure 7: Input and output images of the proposed algorithm using 2D system matrices $\mathbf{SM}_2$ and $\mathbf{SM}_3$. The effect of the grid size of the system matrix can be observed in the reconstructions: grid size a) 19×19 ($\mathbf{SM}_2$) and b) 37×37 ($\mathbf{SM}_3$). Artifacts can be observed in the output image of the algorithm using the grid b), containing the higher number of points since a single pixel can be subtracted more than once when located between the I_{max} of two iterations.
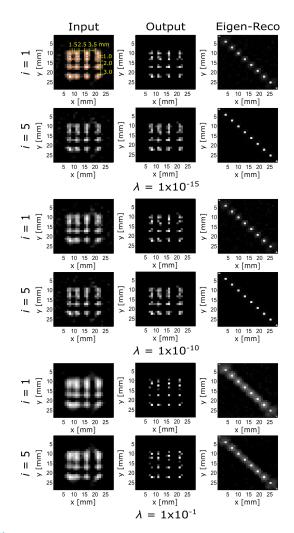

Figure 8: Input (standard reconstruction), output (eigen-reconstruction deblurred), and eigen-reconstructions (sample measurements) for various iteration (i) and regularization (λ) values. Input and output images display the center slices of the reconstructed resolution phantom using $\mathbf{SM}_4$. Deblurring is observed in all output images. The eigen-reconstructions show different intensities and blur levels.

select the stopping criterion can be based on noise levels. Such an approach could provide an automated adaptive threshold which could further reduce user bias and avoid compromising the dynamic range of the signal.

In Figure 6, eigen-reconstructions from $\mathbf{SM}_2$ and $\mathbf{SM}_3$, acquired with Perimag, are shown. There, the effect of the grid size is evident from the intensity and blur. In the eigen-reconstruction of $\mathbf{SM}_2$, the ideal value of 1 was yielded in the center portions of the FoV with virtually no blur. In contrast, a lower intensity with higher blur in the eigen-reconstructed points was found when increasing the number of points in the grid (in $\mathbf{SM}_3$). This suggests that each measurement is not as unique and thus, the signal is shared among a higher number of pixels in the form of noise and blur. Consequently, lower image qual-

ity when reconstructing independent test data can also be expected in this case.

Reconstructions of a shape phantom with an homogeneous concentration can be appreciated in Figure 7. To reconstruct the 2D image, we selected a slice of the 3D grid of probe positions in $\mathbf{SM}_2$ and $\mathbf{SM}_3$, emulating a pure 2D calibration with reduced calibration time. This is a simplified strategy in comparison to the selection of a 2D slice from a 3D reconstructed volume. And while this simplification might not be ideal since the cone covers locations that were not calibrated, standard reconstructions did not show artifacts. Additionally, the strategy allowed the desired relative comparison to the output of our algorithm. For this direct comparison, the resulting images from using a standard reconstruction algorithm (input) are displayed next to the output of the proposed
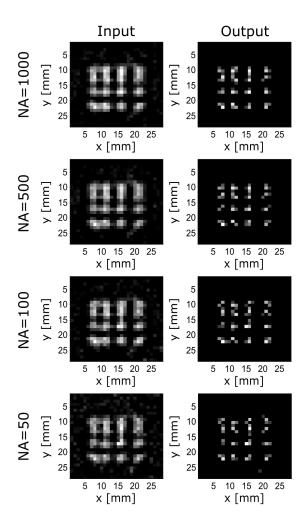
Figure 9: Input (standard reconstruction) and output (eigen-reconstruction deblurred) images from measurement data containing different number of averages (NA). Reconstructions were performed using SM_4 with $i = 1$ and $\lambda = 1 \times 10^{-15}$. Images obtained after applying the deblurring algorithm (output) showed high similarities despite the different noise levels observed in the standard reconstructions.
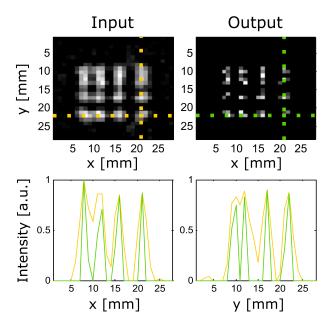

Figure 10: Exemplary input (standard reconstruction) and output (eigen-reconstruction deblurred) images of a resolution phantom with sample profiles. Reconstructions were performed using SM_4 with $i = 1$ and $\lambda = 1 \times 10^{-15}$. Higher intensities and sharper objects can be observed in the profiles of the reconstructed output images in comparison to the input standard reconstruction.

deblurring algorithm. There, a) is the reconstructed data using SM_2, with the grid of 19×19 points whereas b) was reconstructed using SM_3, with the 37×37 grid system matrix. In a), the input image contains higher background noise than the output as this is filtered out by the threshold value of the stopping criterion. Furthermore, no deformations can be observed to the shape of the phantom. On the other hand, artifacts appeared when applying the deblurring algorithm on reconstructions using the higher-point grid system matrix (SM_3). In this case, several points have lower to negligible signal within the object which is not consistent with the real homogeneous distribution of tracer within the phantom. This might occur as a single pixel can be subtracted more than once when located between two pixels recognized as I_{max} in two different iterations. This is a clear

limitation that has to be considered when applying the deblurring algorithm to structures with homogeneous concentrations. Being "hot-spot" technique, MPI often yields sparse images with inhomogeneous concentrations e.g. *in vivo*, it shows no endogenous signal and its tracers do not distribute homogeneously within the body. However, MPI images may neither be as sparse as the point image phantoms nor as homogeneous as the cone phantom in this work. Rather, *in vivo* images will range in between these two extrema which are presented here as boundary conditions. Consequently, the algorithm's performance is expected to oscillate between these two cases with a high dependency on the homogeneity and sharpness of the reconstructed objects. For instance, one should consider that a complex structure could resemble as a point phantom with a low selection field amplitude and a point phantom can be reconstructed as a distribution using high resolutions as demonstrated by the eigen-reconstructions. Moreover, since the deblurring algorithm is an additional process after image reconstruction, it can be directly compared to the input image and opted out of the reconstruction pipeline, for instance when image artifacts are recognized. Rules for the use of the algorithm should be created depending on the quality of the eigen-reconstruction and the sparsity of the images.

The algorithm was also tested on 3D datasets to deblur the reconstructions of a resolution phantom. The
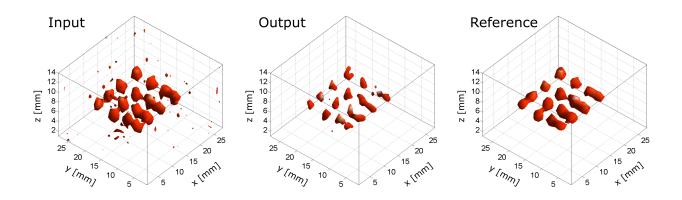
Figure 11: Isosurface representation of the reconstructed 3D volumes of the resolution phantom using **SM**$_4$. The reconstruction followed: a standard Kaczmarz reconstruction with 1 iteration and a regularization factor of 1×10^{-15} (Input), an eigen-reconstruction based iterative deblurring of the input data (Output), and a reference Kaczmarz reconstruction (Reference) using 20 iterations and a regularization factor of 1×10^{-15}. Effective deblurring and noise filtration can be appreciated in the volumes using the proposed algorithm.

results shown in Figure 8 demonstrate the ability to separate objects more clearly in output images compared the standard method (input). Moreover, it can be observed that higher gains from the algorithm were obtained as the blur in the input images increased. As in 2D, this is because the effect of the algorithm will be lessened as the eigen-reconstruction becomes more ideal and the reconstructed voxel is more unique. This effect can be observed also in Figure 8 where exemplary reconstructions using 2 iteration values ($i = 1$, and 5) and three regularization factors ($\lambda = 1 \times 10^{-15}$, 1×10^{-10}, and 1×10^{-1}) are displayed. In 3D, another consideration is the computation time for the algorithm. In this respect, since the algorithm iterates the reconstruction on a point-by-point basis, the reconstruction time can be severely extended. This is mainly controlled by the number of iterations and the threshold value which determines how many voxels will be considered. To compute each voxel above the threshold, the algorithm takes the same amount of time as the standard reconstruction when the reconstruction parameters are unchanged. For instance, the standard reconstruction in Figure 8 ($i = 1$, and $\lambda = 1 \times 10^{-15}$) was performed in ca. 15 seconds, while the eigen-reconstruction algorithm iterated over 70 points for a computation time of ca. 17.5 min. Therefore, it is convenient that the results show efficient deblurring after obtaining the input from the standard reconstruction with a single iteration. In this manner, the reconstruction time can be maintained as low as possible. Parallel computing and regional analysis could also speed up the reconstruction time.

Contrary to a reduced number of iterations of the standard reconstruction, a very high regularization factor there can blur the image beyond the limits of the algorithm and cause artifacts. For instance, 5 points were reconstructed instead of 4 in the vertical direction using

$\lambda = 1 \times 10^{-1}$ (see e.g. 3rd column of dots in the output of $i = 1$, Figure 8).

Using the eigen-reconstruction framework, two sources of image artifacts were identified. First, blurring artifacts arose when the sampling density in the system matrix was increased. This suggests that the particle responses become less distinctive as the separation between probe positioning decreases. Secondly, we identified that the blurring is influenced by the reconstruction parameters namely, the number of iterations and the regularization parameter. This is expected as the reconstruction method solves the least-squares problem by minimizing the norm iteratively and uses the regularization factor to promote smooth varying solutions with less noise. The latter strategy is taken as the system matrix is overdetermined (m > n) and, similarly to the measurement vector, it also includes noise. Therefore, the regularization is used as an attempt to reduce the impact of the noise in the reconstruction under the constraint of maintaining resolved objects.

Figure 9 displays reconstructions resulting from the resolution phantom using measurements with different number of averages. The standard reconstructions (input) showed the expected increased noise level with decreasing number of averages. However, the output images yielded by the deblurring algorithm based on eigen-reconstructions showed high degree of similarity despite the different noise levels in the input images. This indicates that the algorithm is robust for these tested noise levels. Here, the additional feature of noise filtration due to the threshold value of the stopping criteria is evident from the lack of background noise in the output images. Moreover, since the concentration of the tracer affects the signal-to-noise ratio of the image, the robustness of the algorithm to a wide range of signal-to-noise ratios is

an important finding. However, the performance of the algorithm should be reevaluated for *in vivo* studies where the tracer is further diluted, reducing the signal-to-noise ratio.

The deblurring was also evident in profile plots obtained from the standard reconstruction and from the iterative deblurring algorithm based on eigen-reconstructions (see Figure 10). In the profiles, the four objects can be individually observed in both x- and y-axis after deblurring, contrary to the standard reconstruction (input) where objects are partially merged. The noise filtration capabilities of the algorithm can also be observed in the y-axis profiles at 3 mm in comparison to the input image. The quantification of the spatial resolution improvement depends on the input image chosen, which determines the lower limit, and the resolution of the system matrix, which determines the higher limit. In the example presented in Figure 10, the FWHM of the objects in the resolution phantom were a ca. 1.6-fold higher in the input compared to the output image. Moreover, the objects with 1 mm separation can be individually visualized in the profiles of the output images. While this image resolution is still far from the resolution necessary in applications such as the quantification of individual nephrons in rodent kidneys, our approach is a positive step towards maximizing the current capabilities of MPI scanners.

The deblurring and noise filtration can also be observed in the isosurface plots shown in Figure 11 in comparison to the input volume. There, the output 3D volume also demonstrates a higher apparent resolution compared to an standard reconstruction with 20 iterations (Figure 11, Reference).

V. Conclusions

In this work, we demonstrated the application of eigen-reconstructions to evaluate the quality and artifacts of reconstructions based on the system matrix appproach. We also presented and tested an algorithm based on eigen-reconstructions to deblur MPI images. The first important finding is that the eigen-reconstructions of some system matrices are non-ideal and show artifacts. These were deviations in intensity and blur from the ideal reconstruction of a selected measurement with the system matrix where the measurement is also contained. This occurs despite the fact that the selected measurement has an exact match of signal and noise in the system matrix. These artifacts were diminished with parameter optimization following eigen-reconstructions. Thus, the potential of eigen-reconstructions as a testing tool for the system matrix and standard reconstruction algorithm was demonstrated. Moreover, these image artifacts present in the eigen-reconstructions are also expected in the test data and can be compensated.

Our proposed algorithm decreased image blurring effectively thus, increasing apparent spatial resolutions. This suggests that the blur in the system matrix correlates with the blur of the image data. However, limitations were also found when reconstructing an homogeneous structure. Although more sparse and varied contrasts are expected in MPI measurements *in vivo*, eigen-reconstructions should be applied carefully e.g. rules for the use of deblurring could be created depending on the application. In terms of testing, we expect the use of eigen-reconstructions to be adopted and used routinely to ensure system matrix and reconstruction quality. Moreover, the proposed algorithm could be applied to compensate for added blur and noise filtration during the reconstruction.

Acknowledgments

References

[1] J. Weizenecker, B. Gleich, J. Rahmer, H. Dahnke, and J. Borgert. Three-dimensional real-time in vivo magnetic particle imaging. *Physics in Medicine and Biology*, 54(5):L1–L10, 2009, doi:10.1088/0031-9155/54/5/L01.

[2] J. Franke, N. Baxan, H. Lehr, U. Heinen, S. Reinartz, J. Schnorr, M. Heidenreich, F. Kiessling, and V. Schulz. Hybrid MPI-MRI System for Dual-Modal In Situ Cardiovascular Assessments of Real-Time 3D Blood Flow Quantification - A Pre-Clinical In Vivo Feasibility Investigation. *IEEE Transactions on Medical Imaging*, 39(12):4335–4345, 2020, doi:10.1109/TMI.2020.3017160.

[3] E. U. Saritas, P. W. Goodwill, L. R. Croft, J. J. Konkle, K. Lu, B. Zheng, and S. M. Conolly. Magnetic Particle Imaging (MPI) for NMR and MRI researchers. *Journal of Magnetic Resonance*, 229:116–126, 2013, doi:10.1016/j.jmr.2012.11.029.

[4] R. M. Ferguson, A. P. Khandhar, S. J. Kemp, H. Arami, E. U. Saritas, L. R. Croft, J. Konkle, P. W. Goodwill, A. Halkola, J. Rahmer, J. Borgert, S. M. Conolly, and K. M. Krishnan. Magnetic Particle Imaging With Tailored Iron Oxide Nanoparticle Tracers. *IEEE Transactions on Medical Imaging*, 34(5):1077–1084, 2015, doi:10.1109/TMI.2014.2375065.

[5] J. Chacon-Caldera, A. Maunder, M. Rao, G. Norquay, O. I. Rodgers, M. Clemence, C. Puddu, L. R. Schad, and J. M. Wild. Dissolved hyperpolarized xenon-129 MRI in human kidneys. *Magnetic Resonance in Medicine*, 83(1):262–270, 2020, doi:10.1002/mrm.27923.

[6] J. Chacon-Caldera, S. Geraci, P. Krämer, L. Cullen-McEwen, J. F. Bertram, N. Gretz, and L. R. Schad. Fast glomerular quantification of whole ex vivo mouse kidneys using Magnetic Resonance Imaging at 9.4 Tesla. *Zeitschrift für Medizinische Physik*, 26(1):54–62, 2016, doi:10.1016/j.zemedi.2015.12.008.

[7] S. Geraci, J. Chacon-Caldera, L. Cullen-McEwen, L. R. Schad, C. Sticht, V. G. Puelles, J. F. Bertram, and N. Gretz. Combining new tools to assess renal function and morphology: a holistic approach to study the effects of aging and a congenital nephron deficit. *American Journal of Physiology-Renal Physiology*, 313(3):F576–F584, 2017, doi:10.1152/ajprenal.00329.2015.

[8] E. U. Saritas, P. W. Goodwill, G. Z. Zhang, and S. M. Conolly. Magnetostimulation Limits in Magnetic Particle Imaging. *IEEE Transactions on Medical Imaging*, 32(9):1600–1610, 2013, doi:10.1109/TMI.2013.2260764.

[9] J. Chacon-Caldera, H. Lehr, K. Sajjamark, and J. Franke. Eigen-reconstructions: a closer look into the System Matrix. *International Journal on Magnetic Particle Imaging*, 6(2 Suppl. 1), 2020, doi:10.18416/IJMPI.2020.2009072.

[10] B. Gleich and J. Weizenecker. Tomographic imaging using the nonlinear response of magnetic particles. *Nature*, 435(7046):1214–1217, 2005, doi:10.1038/nature03808.

[11] J. Rahmer, J. Weizenecker, B. Gleich, and J. Borgert. Signal encoding in magnetic particle imaging: properties of the system function. *BMC Medical Imaging*, 9:4, 2009, doi:10.1186/1471-2342-9-4.

[12] T. Knopp, J. Rahmer, T. F. Sattel, S. Biederer, J. Weizenecker, B. Gleich, J. Borgert, and T. M. Buzug. Weighted iterative reconstruction for magnetic particle imaging. *Physics in Medicine and Biology*, 55(6):1577–1589, 2010, doi:10.1088/0031-9155/55/6/003.

[13] U. Heinen, A. Weber, J. Franke, H. Lehr, and O. Kosch. A versatile MPI System Function Viewer. *International Journal on Magnetic Particle Imaging*, 3(2), 2017, doi:10.18416/IJMPI.2017.1706006.

[14] T. Knopp, P. Szwargulski, F. Griese, and M. Gräser. OpenMPIData: An initiative for freely accessible magnetic particle imaging data. *Data in Brief*, 28:104971, 2020, doi:10.1016/j.dib.2019.104971.

[15] T. Knopp, T. Viereck, G. Bringout, M. Ahlborg, A. von Gladiss, C. Kaethner, A. Neumann, P. Vogel, J. Rahmer, and M. Möddel. MDF: Magnetic Particle Imaging Data Format. *ArXiv e-prints*, 2019. arXiv: 1602.06072. URL: http://arxiv.org/abs/1602.06072v8.

[16] T. Knopp, P. Szwargulski, F. Griese, M. Grosser, M. Boberg, and M. Möddel. MPIReco.jl: Julia Package for Image Reconstruction in MPI. *International Journal on Magnetic Particle Imaging*, 5(1-2), 2019, doi:10.18416/IJMPI.2019.1907001.

[17] U. Heinen, J. Franke, N. Baxan, K. Strobel, H. Lehr, A. Weber, W. Ruhm, A. P. Khandhar, R. M. Ferguson, S. Kemp, K. M. Krishnan, and M. Heidenreich, Generic multi-purpose multi-modality phantom kit design, in *International Workshop on Magnetic Particle Imaging*, 50, IEEE, 2015. doi:10.1109/IWMPI.2015.7107033.

[18] A. Weber, F. Werner, J. Weizenecker, T. M. Buzug, and T. Knopp. Artifact free reconstruction with the system matrix approach by overscanning the field-free-point trajectory in magnetic particle imaging. *Physics in Medicine and Biology*, 61(2):475–487, 2016, doi:10.1088/0031-9155/61/2/475.